

Modifying La_{0.6}Sr_{0.4}MnO₃ Perovskites with Cr Incorporation for Fast Isothermal CO₂-Splitting Kinetics in Solar-Driven Thermochemical Cycles

*Alfonso J. Carrillo^{a,b+}, Alexander H. Bork^{a,b}, Thierry Moser^{a++}, Eva Sediva^{a,b},
Zachary D. Hood^b, Jennifer L.M. Rupp^{a,b,c*}*

(a) Electrochemical Materials Group, Department of Materials Science, ETH Zurich,
Hönggerberggring 64, 8093 Zürich, Switzerland

(b) Electrochemical Materials Laboratory, Department of Materials Science and
Engineering, Massachusetts Institute of Technology, Cambridge, MA, USA

(c) Electrochemical Materials Laboratory, Department of Electrical Engineering and
Computer Science, Massachusetts Institute of Technology, Cambridge, MA, USA

* Corresponding author: jrupp@mit.edu

+Current address: Instituto de Tecnología Química (Universitat Politècnica de València –
CSIC), Avda. Los Naranjos s/n, 46022 Valencia, Spain

++Current address: Laboratory for Thin Films and Photovoltaics, Empa—Swiss Federal
Laboratories for Materials Science and Technology, Überlandstrasse 129, 8600 Dübendorf,
Switzerland

This is the author manuscript accepted for publication and has undergone full peer review but has not
been through the copyediting, typesetting, pagination and proofreading process, which may lead to
differences between this version and the [Version of Record](https://doi.org/10.1002/aenm.201803886). Please cite this article as [doi:
10.1002/aenm.201803886](https://doi.org/10.1002/aenm.201803886).

This article is protected by copyright. All rights reserved.

Abstract

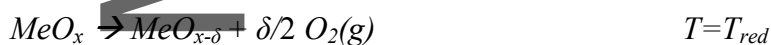
Perovskites are promising oxygen carriers for solar-driven thermochemical fuel production due to higher oxygen exchange capacity. Despite their higher fuel yield capacity, $\text{La}_{0.6}\text{Sr}_{0.4}\text{MnO}_3$ perovskite materials present slow CO_2 splitting kinetics compared with state-of-the-art CeO_2 . In order to improve the CO production rates, we have explored the incorporation of Cr in $\text{La}_{0.6}\text{Sr}_{0.4}\text{MnO}_3$ based on thermodynamic calculations that suggest an enhanced driving force towards CO_2 splitting at high temperatures for $\text{La}_{0.6}\text{Sr}_{0.4}\text{Cr}_x\text{Mn}_{1-x}\text{O}_3$ perovskites. Here, we report a 3-fold faster CO fuel production for $\text{La}_{0.6}\text{Sr}_{0.4}\text{Cr}_{0.85}\text{Mn}_{0.15}\text{O}_3$ compared to conventional $\text{La}_{0.6}\text{Sr}_{0.4}\text{MnO}_3$, and 2-fold faster than CeO_2 under isothermal redox cycling at 1400 °C, and high stability upon long-term cycling without any evidence of microstructural degradation. Our findings suggest that with the proper design in terms of transition metal ion doping, it is possible to adjust perovskite compositions and reactor conditions for improved solar-to-fuel thermochemical production under non-conventional solar-driven thermochemical cycling schemes such as the here presented near isothermal operation.

Keywords

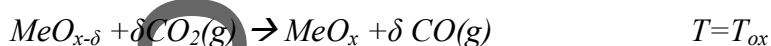
Solar fuels, perovskites, thermochemical, isothermal, kinetics

1. Introduction

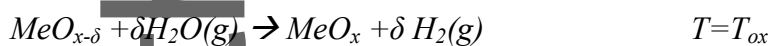
Solar fuels have emerged as a promising path for enabling the transition away from a fossil fuel based economy. Solar energy, the most abundant renewable source on Earth, can be transformed into fuels through several chemical routes.^[1,2] The utilization of concentrated solar energy to drive thermochemical cycles of metal oxides represents an attractive way to produce solar fuels via a 2-step process through which CO₂ and H₂O can be transformed into renewable syngas.^[3-5] In the first step of the process, concentrated solar energy is utilized to thermally reduce an oxide at high temperatures, creating oxygen vacancies, with the consequent release of lattice oxygen, Eq.1. In the second step, conventionally operated at a lower temperature, the reduced form of the metal oxide uptakes oxygen from CO₂ and H₂O injected in the solar reactor, inducing splitting of the reactants by filling the oxygen vacancies of the oxide and producing CO and H₂, commonly referred to as syngas, Eq.2a-b.



Eq.1



Eq.2a



Eq.2b

In order to guarantee the efficiency of the process, the amount of oxygen released (δ) should be high, since it directly correlates with the amount of syngas produced in the second step. In addition, the oxide should show favorable thermodynamics towards splitting of CO₂ and H₂O. Currently, the state-of-the-art material is ceria due to its suitable thermodynamic

properties and fast kinetics for syngas production. Recently, ceria was reported to attain solar-to-fuel efficiencies as high as 5.25%.^[6] Exploring alternative catalysts that provide a higher oxygen release and better splitting kinetics (when compared to that of ceria) is of scientific and technological interest.^[7]

In this respect, perovskite oxides (ABO_3) have attracted much attention due to the plethora of different compositions that can be obtained by doping the A and B-site cations to profit from their oxygen exchange, thermodynamics and splitting kinetics in solar-to-fuel conversion, see a recent review in Ref. ^[8]. Perovskites seem promising due to higher capacity for oxygen release than ceria, which eventually leads to higher CO and H₂ yields. However, the favorable reduction comes at the cost of lower enthalpy and entropy values, which affect the solar-to-fuel efficiency^[4,9] and CO₂ splitting kinetics.^[10,11] Namely, high CO yields were obtained for La_{1-x}Sr_xMnO₃ perovskites (x=0.4), but the decrease in enthalpy of reduction with increasing Sr content^[12] also leads to a lower thermodynamic driving force for fuel production resulting in slower splitting kinetics.^[10,11] Based on the amount of fuel produced per cycle, the La_{0.6}Sr_{0.4}MnO₃ perovskite is still an attractive option for thermochemical syngas production^[10,11,13–20], provided the kinetics and/or thermodynamics are improved. This fact motivated the present work, in which we have explored the partial substitution of Mn by Cr with the purpose of studying its effect on the CO₂ splitting capabilities. This particular perovskite family, which has been focus of study as the anode in Solid Oxides Fuel Cells^[21–23] and in methane conversion towards syngas^[24], has not been evaluated experimentally before for thermochemical solar-to-fuel production. Through very recent computation and thermodynamic equilibrium models based on CALPHAD, it was shown that the composition La_{0.6}Sr_{0.4}Mn_{0.2}Cr_{0.8}O₃ exhibits a comparable solar-to-fuel efficiency of 2.7% when operated for isothermal splitting at 1500 °C to non-transition metal doped La_{0.6}Sr_{0.4}MnO₃, operated for

cycling between 1500°C and 1000°C^[25]. Motivated by this result, this work focuses on the synthesis, phase stability and performance of the solid solution series $\text{La}_{0.6}\text{Sr}_{0.4}\text{Mn}_{1-x}\text{Cr}_x\text{O}_3$ for thermochemical solar-to-fuel conversion. The rationale behind the material choice is illustrated in the Ellingham diagram in Fig. 1, based on data found in the literature.^[26,27] From that thermodynamic data we can extract the Gibbs free energy of oxidation^[28] of $\text{La}_{0.6}\text{Sr}_{0.4}\text{MnO}_{3-\delta}$ and $\text{La}_{0.6}\text{Sr}_{0.4}\text{CrO}_{3-\delta}$, Δg_{ox} for $\delta = 0.1$, and then calculate the Gibbs free energy for the CO_2 splitting reaction with $\text{La}_{0.6}\text{Sr}_{0.4}\text{MnO}_{3-\delta}$ and $\text{La}_{0.6}\text{Sr}_{0.4}\text{CrO}_{3-\delta}$ perovskites, Δg_{rxn} ($\Delta g_{rxn} = \Delta g_{ox\delta=0.1} + \Delta g_{\text{CO}_2}$; where Δg_{CO_2} is the Gibbs free energy for the CO_2 splitting). Solid solutions of $\text{La}_{0.6}\text{Sr}_{0.4}\text{Cr}_x\text{Mn}_{1-x}\text{O}_3$ are expected to have thermodynamic properties, Δg_{rxn} , that lie in between the end members^[8,25,29] Based on this assumption the total Gibbs free energy of the oxidation of the perovskites $\text{La}_{0.6}\text{Sr}_{0.4}\text{Cr}_x\text{Mn}_{1-x}\text{O}_3$ by splitting CO_2 will have a higher absolute value and higher thermodynamic driving force for CO production with a higher concentration of Cr *i.e.* increasing values of x , compared to $\text{La}_{0.6}\text{Sr}_{0.4}\text{MnO}_3$. Importantly, at the working conditions relevant for thermochemical CO_2 splitting, $\text{La}_{0.6}\text{Sr}_{0.4}\text{CrO}_{3-\delta}$ perovskite shows very little oxygen release^[28], thus adjusting the Cr/Mn ratio in $\text{La}_{0.6}\text{Sr}_{0.4}\text{Cr}_x\text{Mn}_{1-x}\text{O}_3$ solid solutions would serve to optimize the tradeoff between oxygen release and enhanced thermodynamic driving force. In addition, under practical solar-to-fuel conditions, the kinetics of the oxidation in perovskites are governed by their *thermodynamic* properties rather than *material kinetic* properties as shown in our previous work on the perovskite $\text{La}_{1-x}\text{Sr}_x\text{MnO}_3$,^[11] and we expect that Cr doping will result in faster fuel production rates based on thermodynamic considerations depicted in Fig.1. Attending at the temperature range at which Δg_{rxn} shows more negative values, this would be especially relevant at high oxidation temperatures, indicating that those compositions would be promising materials for operation under isothermal cycling schemes ($T_{red} = T_{ox}$).

Classically, thermochemical solar-to-fuel cycling is conducted in a two-step thermochemical cycle operating between a reduction and oxidation temperature as highlighted in Equations 1 and 2a-b. The reason for the two steps is that most applied materials such as $\text{La}_{1-x}\text{Sr}_x\text{MnO}_3$ or CeO_2 show optimal CO_2 and H_2O splitting conditions at temperatures below 1000 °C, since the driving force for the splitting reaction^[11,12], *i.e* a more negative Δ_g , increases when lowering the temperature, see Fig. 1. This driving force would be different for Cr-rich $\text{La}_{0.6}\text{Sr}_{0.4}\text{Cr}_x\text{Mn}_{1-x}\text{O}_3$, since the Ellingham plot reveals a more negative $\Delta_{g_{\text{ox}}}$ for $\text{La}_{0.6}\text{Sr}_{0.4}\text{CrO}_3$ at higher temperatures^[25] (1000-1400 °C), see Fig. 1. This information indicates that Cr-rich $\text{La}_{0.6}\text{Sr}_{0.4}\text{Cr}_x\text{Mn}_{1-x}\text{O}_3$ might benefit from isothermal ($T_{\text{red}}=T_{\text{ox}}$) or near-isothermal operation schemes. Isothermal thermochemical fuel production has been experimentally shown for the hercynite cycle in a stagnation flow reactor^[30] and ceria^[31–33], the latter redox-material being tested with lab-scale membrane^[31] and fixed-bed reactors^[32]. Additionally, isothermally CO_2 splitting has been performed with $\text{La}_{1-x}\text{Sr}_x\text{MnO}_3$ and $\text{Y}_{0.5}\text{Sr}_{0.5}\text{MnO}_3$ perovskites in thermobalance, the latter showing an enhanced fuel production at 1300 °C compared to $\text{La}_{0.5}\text{Sr}_{0.5}\text{MnO}_3$.^[34] Operating isothermally or near-isothermally might benefit from faster kinetics and less thermal stresses in the material since temperature changes are not applied, resulting in higher morphological stability^[30,35]. However, to the best of our knowledge, the influence of temperature on the CO_2 and/or H_2O splitting kinetics has not been evaluated at temperatures in the isothermal regime, and existent literature mainly covered kinetic aspects of CO_2 and/or H_2O splitting reactions with Mn-based perovskite materials using temperature-swing 2-step cycling^[10,17,36,37].

Erhart *et al.* carried out a process efficiency analysis pointing out that near-isothermal operation, *e.g* $\Delta T = T_{\text{red}} - T_{\text{ox}} \sim 100\text{-}200$ °C, might be the most optimal scheme for materials with slow kinetics,^[38] although the most optimum temperature interval for a given system would

depend on the intrinsic thermodynamic and kinetic properties of each material. Furthermore, isothermal cycling shows several operational benefits, such as reduced downtime, since cooling down is avoided, and easier solid-solid heat recuperation can be established.^[35]

In conclusion, thermodynamic considerations indicate that the new material candidate $\text{La}_{0.6}\text{Sr}_{0.4}\text{Cr}_x\text{Mn}_{1-x}\text{O}_3$ is supposed to benefit from operation in the near-isothermal to isothermal temperature range, but requires first experimental proof by synthesis and experimental validation of performance characteristics and stability for thermochemical solar-to-fuel conversion.

2. Results

2.1. Structural characterization of $\text{La}_{0.6}\text{Sr}_{0.4}\text{Cr}_x\text{Mn}_{1-x}\text{O}_3$ perovskite materials

In this work, $\text{La}_{0.6}\text{Sr}_{0.4}\text{Cr}_x\text{Mn}_{1-x}\text{O}_3$ materials, with chromium concentrations of $x=0-0.85$ for the solid solution, were synthesized via the Pechini method. XRD patterns of the pristine samples showed that after calcination at 1400 °C for 24h, all the materials, regardless of the Cr content, exhibited rhombohedral crystal structure (space group $R - \bar{3}c$) without the presence of any detectable phase segregation, see Fig.2 and Table 1. Progressive Mn cation replacement by Cr on the transition metal ion perovskite site led to a shift of X-ray signatures to higher 2θ values as observed in the grey shadowed area around 47°, zoomed in Fig.1, indicating lattice shrinkage. To verify it and probe whether all synthesized materials reveal full solid solution mixing we determined the crystallographic cell volume evolution over the change in Cr-doping concentration, Fig.3a. All values of the lattice volume were obtained by Rietveld refinement, as exemplified for $\text{La}_{0.6}\text{Sr}_{0.4}\text{Cr}_{0.3}\text{Mn}_{0.7}\text{O}_3$ in Supporting Information Fig.S1. We report for up to 50% of chromium doping on the transition metal ion site ($x=0.5$),

a linear decrease of the cell volume with increasing Cr content, in agreement with Vegard's law^[39]. This result correlates well with a partial substitution of Mn^{3+} , $r_{\text{Mn}^{3+}}=0.645$ nm in 6-fold coordination, by Cr^{3+} being of smaller ionic radius size, $r_{\text{Cr}^{3+}}=0.615$ nm. For higher chromium concentrations a deviation from Vegard's law exists and cell volume stagnates at around 344 \AA^3 . The observation that Vegard's law is only followed up to an equal doping level of chromium and manganese for the perovskite, while keeping the same crystallographic phase might point to a potential valence change of the chromium; viz. partial substitution of Cr^{3+} by Cr^{4+} ($r_{\text{Cr}^{4+}}=0.55$ nm, $r_{\text{Cr}^{3+}}=0.615$ nm in 6-fold coordination)^[40]. Earlier studies on Sr and Ni-doped lanthanum chromates have pointed to an increased presence of Cr^{4+} in Temperature-programmed Reduction (TPR) and XPS measurements^[41].

To probe this hypothesis, we turn to Raman spectroscopy analyzing the near order structural characteristics of the perovskite solid solutions, Fig.3b. The Raman spectrum of the rhombohedral $\text{La}_{0.6}\text{Sr}_{0.4}\text{MnO}_3$ shows three broad peaks in the region between 400 and 700 cm^{-1} Fig.3b. Such modes have been observed in rhombohedral rare earth-doped manganites and were ascribed to the oxygen sub-lattice disorder^[42] created by the incoherent Jahn-Teller distortions around Mn^{3+} (d^4). We measure that these Raman modes gradually develop into two sharper bands at 488 and 593 cm^{-1} when adding Cr, which we ascribe to E_g modes of the rhombohedral LaCrO_3 according to Iliev *et al.*^[43]. The low-frequency mode around 200 cm^{-1} we ascribe to the A_{1g} mode of the rhombohedral structure according to Dubroka *et al.*^[44] When doping with 10 mol% Cr, $x=0.1$, a new band around 715 cm^{-1} emerges, which grows and shifts to lower wavenumbers when increasing the Cr content, Fig.3c. The strong mode around 720 cm^{-1} is in accordance with previously reported Raman spectra of $\text{La}_{1-y}\text{Sr}_y\text{Cr}_{0.1}\text{Mn}_{0.9}\text{O}_3$ ^[44] and could be ascribed according to structurally related perovskite solid solutions^[45–51] to a A_g -like local oxygen breathing mode. Cr^{4+} causes a Jahn-Teller distortion

of the $(\text{Cr}^{4+})\text{-O}_6$ octahedron, which can create the local lattice distortion activating the 720 cm^{-1} mode, see Ref. [42] for details on the example of LaCrO_3 . However, the intensity of the mode, Fig.3c, follows the expected concentration of Cr^{3+} , rising until $x=0.75$ as Cr^{3+} replaces Mn^{3+} . Interestingly, for $x=0.85$, the relative peak intensity drops again to a lower value than for $x=0.75$ (48.15 and 57 a.u. respectively), indicating a lower presence of Cr^{4+} in $x=0.85$ than in $x=0.75$, which would correlate well with a slightly larger cell volume for $x=0.85$, (344.22 \AA^3) than $x=0.75$ (343.94 \AA^3). Although we cannot conclusively ascribe the mode at $715\text{-}740\text{ cm}^{-1}$ to Cr^{4+} or Cr^{3+} based on these Raman observations and those reported in the literature, the correlation between the peak intensity of the A_g -like mode and the Cr content can point to an increase of the $\text{Cr}^{4+}/\text{Cr}^{3+}$ ratio with increasing Cr content for the $\text{La}_{0.6}\text{Sr}_{0.4}\text{Cr}_x\text{Mn}_{1-x}\text{O}_3$ materials. In addition, we confirmed the presence of Cr^{4+} by XPS in the surface of $\text{La}_{0.6}\text{Sr}_{0.4}\text{Cr}_{0.85}\text{Mn}_{0.15}\text{O}_3$ before and after a thermochemical durability cycle. These results are discussed in detail in section 2.3.

Collectively, we conclude that for doping up to $x=0.5$ a full solid solution prevails in the material. Doping beyond $x=0.75$ the Cr concentration maintains the rhombohedral structure, however, XRD and Raman analysis of the A_g -like mode point to a progressing Jahn-Teller distortion and change in the chromium valence change with a higher Cr^{4+} concentration

Fig.3d displays the oxygen release, δ , during reduction under Ar up to $1400\text{ }^\circ\text{C}$ of the perovskite powders in a thermogravimetric analyzer. Introducing more Cr dopants on the transition metal ion position of the manganese results in a generally lowered oxygen release. For example, it reduces from $\delta \sim 0.037$ at $x=0$ to $\delta \sim 0.01$ for $x=0.75\text{-}0.85$, Fig. 3d; this result would also imply a lower fuel production capacity for the water or CO_2 splitting step, Eq.2a. The lowered oxygen exchange with increasing Cr content in $\text{La}_{0.6}\text{Sr}_{0.4}\text{Cr}_x\text{Mn}_{1-x}\text{O}_3$ agrees well

with thermodynamic data in the literature, indicating that lanthanum chromates require more reducing conditions to release oxygen.^[8] The lower oxygen release is ascribed to the higher presence of less reducible Cr⁴⁺ cations, in agreement with the XRD and Raman observations.

The influence of Cr-doping on the microstructure was studied by SEM, Fig.4. It was observed that incorporation of chromium, as low as x=0.1, induced particle growth compared to pure La_{0.6}Sr_{0.4}MnO₃. The average grain size increases from 1.5±0.5 to 2.5±0.7 μm, for increase of chromium to x=0.3, Fig.4b, Table 1. Similar behavior was found in literature for (Sr_{0.7}Ce_{0.3})_{1-x}Mn_{1-y}Cr_yO_{3-δ}, where authors reported grain sizes of 1-4 μm for y=0 to 7-14 for y=0.5.^[52] Additionally Saravanan et al. observed an increase in grain growth with an increase in Cr content on (La_{0.8}Ca_{0.2})(Cr_{0.9-x}Co_{0.1}Mn_x)O₃ perovskites, viz. 0.666 μm for x=0.03 and 0.351 μm for x=0.12.^[53] In these reports, the authors ascribed the particle growth to Cr incorporation. One possible explanation can be related with the presence of Cr that during the high-temperature processing can form volatile species such as CrO₃ that then are deposited again on the surface of the perovskite phase forming SrCrO₄ nuclei, which act as nucleation sites for the eventual perovskite particle growth^[54,55]. Interestingly, when increasing the Cr content up to x=0.85, Fig.3f, average grain size decrease by 30% to 1.7±0.6 μm. Notably this decrease in grain size is accompanied by a slightly higher presence of intergranular pores and also a higher degree of grain faceting is exhibited, Fig.4f. Through the following, we test the compositions of La_{0.6}Sr_{0.4}Cr_xMn_{1-x}O₃ for thermochemical cycling and also comment on the microstructure evolution during testing.

2.2. Thermochemical fuel production and CO₂ splitting kinetics

After identifying the implications of Cr-incorporation on the physicochemical properties of these perovskites, we turn to the investigation of the fuel production performance. Through this study, we evaluated thermochemical splitting cycles for $\text{La}_{0.6}\text{Sr}_{0.4}\text{Cr}_x\text{Mn}_{1-x}\text{O}_3$ at both near-isothermal and isothermal conditions, for which we exemplify on the splitting of CO_2 , tested in a high-temperature fixed bed reactor, see Experimental Methods for more details. Importantly, we will compare the rate production and CO yields with two of the state-of-the-art materials, the perovskite $\text{La}_{0.6}\text{Sr}_{0.4}\text{MnO}_3$ and CeO_2 .

Thermochemical cycling tests were performed to the $\text{La}_{0.6}\text{Sr}_{0.4}\text{Cr}_x\text{Mn}_{1-x}\text{O}_3$ materials from $x=0$ to $x=0.85$, in which O_2 release and CO production were monitored for eight consecutive cycles, evaluating the influence of the reduction (1200, 1300 and 1400 °C) and oxidation temperatures (1000-1400 °C), Fig.S2 in the Supporting Information, showing that for every temperature and cycle tested, all the $\text{La}_{0.6}\text{Sr}_{0.4}\text{Cr}_x\text{Mn}_{1-x}\text{O}_3$ perovskite materials exhibited O_2 and CO production in the reduction/oxidation cycles, respectively. The results obtained during the first three isothermal cycles reflect that performing reduction at higher temperatures leads to higher O_2 release and, thus, higher CO production for every sample, indicating that 1400 °C is the most suitable temperature for isothermal cycling for this family of perovskites. For each material, the temperature increase leads also to faster CO production rate. For instance, for $\text{La}_{0.6}\text{Sr}_{0.4}\text{Cr}_{0.3}\text{Mn}_{0.7}\text{O}_3$, the CO peak rate increases from $0.17 \text{ mL min}^{-1} \text{ g}^{-1}$ at 1200 °C to $1.14 \text{ mL min}^{-1} \text{ g}^{-1}$ at 1400 °C.

Interestingly, we observed that isothermal CO_2 splitting, especially at 1300 and 1400 °C, generates concomitantly O_2 . The source of O_2 production during CO_2 splitting is ascribed to the thermolysis of CO_2 ($\text{CO}_2 \rightarrow \text{CO} + 1/2\text{O}_2$), mainly catalyzed by the alumina reactor inner surface and the powder bed at high temperatures, see Fig.S3 Supporting Information. This effect has been reported for isothermal H_2 and CO production with ceria^[31,33] and

hercynite^[56], however, this is the first observation of this kind for isothermal cycling of perovskites, since previous studies rely on thermogravimetric analysis^[34,57] that cannot monitor catalytic processes unrelated to weight changes. The thermolysis contribution to CO production was subtracted from the total CO generated in order to analyze the performance of $\text{La}_{0.6}\text{Sr}_{0.4}\text{Cr}_x\text{Mn}_{1-x}\text{O}_3$ perovskites under isothermal CO_2 splitting. Fig.5a depicts the total CO produced isothermally at 1400 °C, differentiating both sources, thermolysis and CO_2 splitting. The highest fuel production was observed for $x=0.1$, with 3.3 mL g^{-1} of CO, although $x=0.3$ -0.75 exhibited close performance with CO production around 2.9 mL g^{-1} . The compositional ends $x=0$ and $x=0.85$ showed the lowest production with values below 2 mL g^{-1} . Here, it should be pointed out that our cycling tests were designed with shorter exposure to CO_2 to evaluate the kinetics with respect to the Cr concentration in the perovskite material. It is important to note that the materials are exposed to CO_2 for 20 min instead of commonly reported 40-60 min in literature^[10,11]. Because of the shorter oxidation time, the total CO production and CO/O_2 molar ratios for $\text{La}_{0.6}\text{Sr}_{0.4}\text{MnO}_3$ are generally lower when compared to literature. However, for future reactor operation these short time ranges are of relevance, as shorter oxidation times allow for practical reactor operation at increased efficiency.^[11] It can be seen in Fig.5b that $\text{La}_{0.6}\text{Sr}_{0.4}\text{MnO}_3$ exhibits a 3-fold higher oxygen exchange capacity than $\text{La}_{0.6}\text{Sr}_{0.4}\text{Cr}_{0.85}\text{Mn}_{0.15}\text{O}_3$. However, this material did not show the highest CO yields because it requires longer exposure to CO_2 , as previously demonstrated in the literature^[10,11]. This result illustrates the importance of finding a trade-off between materials with high yields that require short exposure to CO_2 to affect process efficiency towards flexible operation schemes. Perovskites normally require a larger excess of gaseous oxidant, when compared to that of ceria^[58], and it may even be more relevant to assure ideal exposure time in oxidation step. In this respect, under the experimental conditions used for this work, the optimum CO yield production was observed for $x=0.3$ at 1200 °C, with 4.6 mL g^{-1} , Fig.5c, showing the

best CO production under any of the temperature-swing cycling tests conducted, indicating that for such composition a trade-off between oxygen capacity and CO₂ splitting rates was attained. Interestingly, for all the compositions the amount of fuel produced at 1300 °C, Fig.5c, was lower than at values obtained at 1200 °C, which for Cr-rich compositions is counterintuitive given the expected increase of fuel yields with temperature on the basis of reported thermodynamic trends on Fig.1. For instance, La_{0.6}Sr_{0.4}Cr_{0.75}Mn_{0.25}O₃ shows 2.49 mL g⁻¹ at 1200 °C, 1.88 mL g⁻¹ at 1300 °C and 2.89 mL g⁻¹ at 1400 °C. Although the general trend indicates that the fuel yield increases with temperature, the value at 1300 °C lies below that trend. We ascribed this anomalous result to the underestimation of CO coming from CO₂ splitting caused by subtraction of CO coming from the CO₂ thermolysis source, an effect that is even more pronounced for La_{0.6}Sr_{0.4}Cr_{0.85}Mn_{0.15}O₃ due to inherently lower oxygen exchange capacity and smaller fuel increase changes with temperature. Importantly, this fact does not alter the kinetic trends described in the following sections. However, if the amount of CO produced by thermolysis is also computed, then the highest production will be for La_{0.6}Sr_{0.4}Cr_{0.75}Mn_{0.25}O₃ at 1400 °C, which is ca. 7 mL g⁻¹. Direct thermolysis has been recently tested by Jiang et al. and Tou et al.^[31,59], finding in both cases that use of metal oxides that operate on the basis of oxygen vacancy formation enhance the amount of CO produce by direct thermolysis compared to inert materials such as Al₂O₃. The use of a membrane reactor as demonstrated by Tou et al. can be useful for separating the concomitant O₂ produced by CO₂ thermolysis.^[31] Thus, our results suggest that La_{0.6}Sr_{0.4}Cr_{0.75}Mn_{0.25}O₃ composition could be a promising candidate to be used as a membrane reactor for redox-augmented direct thermolysis, although some concerns respect to thermodynamic limitations of membrane reactors for direct thermolysis have been raised recently.^[60]

We turn now to the last five cycles, in order to analyze in more detail, the effect of Cr-incorporation and temperature on the CO₂ splitting kinetics. In this case, the reduction temperature was maintained at 1400 °C for every half-cycle in order to guarantee the same extent of oxygen vacancy formation for each temperature at which the CO₂ splitting reaction was evaluated. In order to compare more clearly the influence of the Cr content to the kinetics, we plot the CO rate production curve for the samples with the lowest (x=0 and x=0.1) and highest (x=0.75 and x=0.85) amount of Cr on the transition metal-site, extracted from the CO₂ splitting reaction at 1200 °C, Fig.6. It can be observed that for Cr x=0.85, a peak rate of 0.93 mL min⁻¹ g⁻¹ is achieved, which is almost a 3-fold improvement compared to La_{0.6}Sr_{0.4}MnO₃, 0.33 mL min⁻¹ g⁻¹. A faster kinetic performance is also confirmed by the shorter time needed for reaching equilibrium CO production, which is just 8 min for Cr x=0.85, whereas for Cr x=0 the material did not even reach equilibrium during the 20 min of CO₂ injection. To put this result in perspective, more commonly used La_{0.6}Sr_{0.4}MnO₃ would require about more than one hour to reach equilibrium with a fuel production of 8.9 mL g⁻¹.^[10] A peak rate of 0.52 mL min⁻¹ g⁻¹ was observed for the perovskite with Cr content x=0.1, however, it also did not reach equilibrium in the given splitting reaction time. In contrast, this was almost achieved by La_{0.6}Sr_{0.4}Cr_{0.75}Mn_{0.25}O₃ in the 20 min given for the CO₂ splitting reaction, depicting a peak rate value of 0.8 mL min⁻¹ g⁻¹. Here, it should be noted that La_{0.6}Sr_{0.4}Cr_{0.5}Mn_{0.5}O₃ exhibited a peak rate value that lies below the trend displayed by the other five compositions Fig.S2. Ignoring this outlier, Fig.6 depicts an increased CO production rate with increasing Cr-incorporation on the transition metal-site by comparing the compositional end-members, illustrating the positive influence of Cr-doping on improving the CO₂ splitting kinetics. Additionally, the results indicate that it could be possible to design a more efficient material by modulating the Cr-content in order to optimize the CO₂ splitting reaction time. This is especially relevant considering the excess of oxidant

gas required by perovskites^[58] which leads to low CO₂ to CO total conversions^[10]. This fact would also affect the CO/CO₂ separation costs, although Marxer et al. determined it to be 1% of the syngas high heating value^[61]. In terms of CO/CO₂ volume concentration peak values range from the highest 1 % (v/v) (average 0.2 % (v/v) per cycle) for La_{0.6}Sr_{0.4}Cr_{0.85}Mn_{0.15}O₃ at 1400 °C, to the lowest 0.12 % (v/v) (average 0.05 % (v/v) per cycle) for La_{0.6}Sr_{0.4}MnO₃ at 1000 °C, although it should be noted that experimental conditions were not optimized to favor high CO/CO₂ volume concentration in the present study. Provided these facts, strategies for more efficient fuel production have been suggested, indicating that limiting the CO₂ splitting reaction time would be preferable instead of targeting a maximum fuel output per cycle as preference^[10]. This trend again points out the need to find perovskite oxides in which not only a high fuel (CO and/or H₂) yield per cycle is achieved, but also materials that exhibit fast CO₂ splitting rates, since excess of gaseous reactant is required, which will add energy penalties in the CO/CO₂ separation.

Next, we analyze the influence of temperature at isothermal and near-isothermal relevant temperatures for the end compositions $x=0$ and $x=0.85$, and $x=0.5$, benchmarked against CeO₂, the reference material in thermochemical solar-to-fuel production, Fig.7a. For that purpose, commercial CeO₂, was subjected to the same thermochemical cycling tests as the perovskite powders, see Fig.S4. CeO₂ is well known to have extremely fast kinetics, especially compared with La_{0.6}Sr_{0.4}MnO₃ materials, which might be considered the reference perovskite material for thermochemical solar-to-fuel production.^[11] Our experiments revealed that an increase in the CO₂ splitting temperature resulted in a remarkable exponential decay of the peak rate for CeO₂. Specifically, it decreases by more than three times of its initial rate, 3.1 mL min⁻¹ g⁻¹ at 1200 °C, to 0.8 mL min⁻¹ g⁻¹ at 1400 °C, keeping the reduction

temperature at 1400 °C in both cases. Contrarily, $\text{La}_{0.6}\text{Sr}_{0.4}\text{Cr}_x\text{Mn}_{1-x}\text{O}_3$ materials improved their kinetic performance with an increase of the CO_2 splitting temperature in a linear fashion.

In this work we report first temperature-dependent kinetic trends for perovskites of the family $\text{La}_{0.6}\text{Sr}_{0.4}\text{Cr}_x\text{Mn}_{1-x}\text{O}_3$ at near-isothermal and isothermal regimes. Most of current literature investigates perovskite oxides only in temperature-swing cycling operation. For example, we only found a similar work for hercynite, which exhibited faster CO_2 splitting rates with increased isothermal temperature^[56], ascribed to a higher reduction extent with increased temperature. They argued that a higher reduction extent, increases the oxidation driving force due to an enhanced favorability for CO production. This kinetic behavior reported by Muhich et al., matches well for both the perovskite, see Fig.S2, and ceria, see Fig.S4, behavior with increasing isothermal temperature, that is the three first cycles of our thermochemical cycling program. Interestingly, this behavior does not apply for ceria when cycled between two different temperatures, *i.e.* $T_{\text{red}}=1400$ °C and $T_{\text{ox}}=1000\text{-}1300$ °C. In this case, the reduction extent is to some degree fixed, and ceria shows a higher favorability for splitting CO_2 at lower temperatures, exhibiting a slowdown when the oxidation temperature is increased as shown in Fig.7a. This is ascribed to the thermodynamics of ceria, which shows a high gain in thermodynamic driving force with cooling^[62], that is, faster CO rates at lower temperatures and decay at high temperatures (1000-1400 °C) as shown in Fig.7a and Fig.S4, corroborating the trends reported by Davenport et al.^[63] On the other hand, the $\text{La}_{0.6}\text{Sr}_{0.4}\text{Cr}_x\text{Mn}_{1-x}\text{O}_3$ series exhibit the opposite behavior.

Fundamentally this finding is in line with the theoretical trend illustrated in Fig.1 that depicts an increased CO_2 -splitting thermodynamic driving force, Δg_{rxn} , for samples with high chromium content in the high temperature regime. Turning to Fig.7a again, it can be seen that

the rate enhancement with temperature can be ranked in the following way: $x=0.85 > x=0.5 > x=0$; which can be observed by a steeper slope for the linear trend of CO rates with temperature (red, green and blue lines, respectively). While this corroborates that the driving force gain is higher for Cr-rich perovskites than for $\text{La}_{0.6}\text{Sr}_{0.4}\text{MnO}_3$, it would be expected a higher CO production rate difference in favor of $x=0.85$ at high temperatures, and increased rate values for $\text{La}_{0.6}\text{Sr}_{0.4}\text{MnO}_3$ when decreasing the temperature. One possible reason for this behavior can be explained by the rationale of Muhich et al., mentioned above, which ascribed higher CO_2 splitting driving force for increased reduction extents for hercynite. Here, we note that for temperature-swing cycles, the higher the temperature difference between T_{red} and T_{ox} , the longer it took to reach the set-point oxidation temperature. Namely, it took ca. 20 min to cool down from 1400 °C to 1000 °C, while just 2 min from 1400 to 1300 °C. Although the same cooling rate was programed for both, 50 °C min^{-1} , the electric-furnace thermal inertia caused an exponential cooling down, see the top-panel in Fig.S2, that delayed reaching 1000 °C by 12 min more. During cooling, the metal oxide will be reoxidized slightly from residual oxygen in the inert gas stream, which decreases the reduction extent δ before CO_2 splitting, phenomenon previously reported by Cooper et al.^[57], being this alteration negligible for near-isothermal schemes. Other authors avoided this artifact by using rapid-cooling IR furnaces.^[10] This hypothesis could serve to explain why the reported CO yields, Fig.5a, are much lower for 1000 °C. Reoxidation will also affect the reduction extent of ceria but less on its reoxidation kinetics, Fig.7a and Fig.S4. The reason is again explained by thermodynamic trends, since the driving force for CO_2 splitting for ceria strongly increases with decreasing the temperature, while the driving force for splitting is not affected to the same degree by lowering the oxygen non-stoichiometry, δ .^[62] This fact once more emphasizes the importance of the reported trends in this work. That is, for the isothermal reactor operation, in which $T_{red}=T_{ox}=1400$ °C, $\text{La}_{0.6}\text{Sr}_{0.4}\text{Cr}_{0.85}\text{Mn}_{0.15}\text{O}_3$

exhibits a 2-fold faster fuel production rate compared to CeO_2 , being at 1.5 and 0.8 $\text{mL min}^{-1} \text{g}^{-1}$, respectively, Fig.7b. This result indicates that by adjusting both the perovskite composition and reactor operational scheme, it is possible to find material alternatives that outperform state-of-the-art perovskites, such as $\text{La}_{0.6}\text{Sr}_{0.4}\text{MnO}_3$, and more importantly, ceria. Thus, it is demonstrated that $\text{La}_{0.6}\text{Sr}_{0.4}\text{Cr}_x\text{Mn}_{1-x}\text{O}_3$ solid solutions are promising candidates for renewable fuel production at isothermal and near-isothermal operation. Importantly, such cycling schemes will reduce process downtimes (cooling down), avoid solid-solid heat recuperation, and mitigate thermal stresses, for both the reactor and redox material.^[64]

In order to assess the microstructural and crystallographic stability, XRD, SEM and EDX were performed to the samples after the cycling tests. XRD analyses, Fig.S5 of the Supporting Information, confirmed that the rhombohedral perovskite structure is the single phase present after cycling, without further evidence of phase segregation for all the Cr-doped, $x=0.1-0.85$, $\text{La}_{0.6}\text{Sr}_{0.4}\text{Cr}_x\text{Mn}_{1-x}\text{O}_3$ perovskite materials. Furthermore, the cell volume values remained almost constant after cycling, and following the same trend as for the pristine samples, Fig.3a, for all the compositional series denoting high crystallographic stability. Upon cycling, SEM micrographs, Fig.4i-h, revealed that Cr-doped materials showed remarkable morphological stability given the prolonged thermochemical treatment at high temperatures, except for $\text{La}_{0.6}\text{Sr}_{0.4}\text{MnO}_3$, Fig.4g, whose particles grow from $1.5\pm0.5 \mu\text{m}$ before cycling to $3\pm0.5 \mu\text{m}$ after the thermochemical cycling tests. Interestingly, $\text{La}_{0.6}\text{Sr}_{0.4}\text{MnO}_3$ was composed of a smaller average grain size ($1.5\pm0.5 \mu\text{m}$ vs. $2.5\pm0.7 \mu\text{m}$ for $\text{La}_{0.6}\text{Sr}_{0.4}\text{Cr}_{0.3}\text{Mn}_{0.7}\text{O}_3$), more bimodal distribution, some closed porosity and a higher rounding degree of the sintered particles as depicted in Fig.4a. This observation is important, since this composition exhibited the slowest CO production at the isothermal test conditions. This result denotes that a lower level of compaction exists for the undoped chromium case of

the perovskite revealing a smaller grain size and also a more open micro-structure. This accounts for higher surface areas, however, in this case, it does not necessarily correlate with faster kinetics. This fact indicates that at the high temperatures of the isothermal CO₂ splitting cycles, the reaction is less controlled by diffusion or surface kinetics, but highly influenced by thermodynamic driving forces. However, an additional study assessing surface modifications of these materials should be performed to corroborate the aforementioned observations.

Furthermore, the presence of small precipitates was observed along some grain boundaries, although the low concentration prevents from detection of such phase using XRD, Fig.S5 in the Supporting Information. Based on the observed lower degree of morphological alteration after the severe thermochemical cycling, we could conclude that Cr-doping could be beneficial in preventing sintering-related effects. These results together with the microstructural durability of La_{0.6}Sr_{0.4}Cr_xMn_{1-x}O₃ powders with x=0.1-0.85 suggests the beneficial effect of Cr-doping preventing materials degradation at high-temperature thermochemical cycling conditions.

2.3. Longevity test under high-temperature isothermal cycling

Finally, the thermochemical longevity performance of the La_{0.6}Sr_{0.4}Cr_xMn_{1-x}O₃ materials was tested under 15 isothermal redox cycles carried out for La_{0.6}Sr_{0.4}Cr_{0.85}Mn_{0.15}O₃ at 1400 °C, Fig.8a. Here, it can be observed that after the first four cycles, CO production rates stabilized around values of 1.65±0.05 mL min⁻¹ g⁻¹, which lies in the range of the CO₂ splitting rates observed for the same material at 1400 °C, Fig.7. This fact illustrates the reproducibility of the splitting results and the remarkable kinetic stability of La_{0.6}Sr_{0.4}Cr_{0.85}Mn_{0.15}O₃ under high-

temperature isothermal CO₂ splitting cycling schemes. Interestingly, the area under the tail of the CO signal decreased with cycling, an effect that was more pronounced during the first four cycles. This result indicates a cycle-to-cycle decline in the amount of CO produced by thermolysis. The fact that the CO originated by thermocatalytic splitting decreases with time might be ascribed to a reduction of active perovskite surface due to high-temperature sintering effects.

SEM was used in order to analyze the microstructural changes after such prolonged isothermal cycling test and explore this hypothesis. The morphology evolution is depicted in Fig.8b and Fig.8c, depicting La_{0.6}Sr_{0.4}Cr_{0.85}Mn_{0.15}O₃ before and after the 15 cycles, respectively. The comparison of the two micrographs shows that after cycling, the particle grains exhibited an enhanced rounding degree, Fig.8c, in comparison with the sharper edges before cycling, Fig.8b. This result could explain the aforementioned lower thermocatalytic activity since the rounded particles might have less active sites for CO₂ thermolysis due to the partial decrease of surface area. The average grain size values of both the material before and after cycling lie around the same values, 1.7±0.6 μm, which might indicate that, besides the grain rounding, La_{0.6}Sr_{0.4}Cr_{0.85}Mn_{0.15}O₃ maintains remarkable microstructural stability after 15 isothermal CO₂ splitting redox cycles at 1400 °C. Durability is also crucial, considering that redox materials for solar-driven thermochemical syngas production are going to be exposed to long-term cycling at high temperatures, in order to guarantee the feasibility of the process. EDX elemental mapping performed to La_{0.6}Sr_{0.4}Cr_{0.85}Mn_{0.15}O₃ revealed a uniform ionic distribution after the 15 redox isothermal cycles, Fig.8d. Additionally, XRD confirmed that rhombohedral perovskite is the solely crystal phase present in the material after the durability test at 1400 °C, Fig.S6 in the Supporting Information.

X-ray photoelectron spectroscopy (XPS) was also used to compare the chemical stability and to probe any changes in the valence states and their proportions in $\text{La}_{0.6}\text{Sr}_{0.4}\text{Cr}_{0.85}\text{Mn}_{0.15}\text{O}_3$ prior to and after 15 isothermal cycles carried out isothermally at the maximum temperature of 1400 °C. In particular, we focus on the high-resolution XPS of the $\text{Cr}2p_{1/2}$ and $\text{Cr}2p_{3/2}$; and $\text{Mn}2p_{3/2}$ and $\text{Mn}2p_{1/2}$ regions in order to study the surface stability of the multivalent redox cations present in the perovskite, see Fig.8e. Each $\text{Cr}2p$ spectrum was fitted using spin-orbital doublets centered at 576.1 and 585.9 eV ascribed respectively to $\text{Cr}2p_{3/2}$ and $\text{Cr}2p_{1/2}$ of Cr^{3+} , spin-orbital doublets centered at 577.1 and 586.8 eV attributed respectively to $\text{Cr}2p_{3/2}$ and $\text{Cr}2p_{1/2}$ of Cr^{4+} , and spin-orbital doublets centered at 580.0 and 589.5 eV respectively due to $\text{Cr}2p_{3/2}$ and $\text{Cr}2p_{1/2}$ of Cr^{6+} .^[65,66] Importantly, the presence of Cr^{4+} , in both the cycled and the pristine samples, confirms our XRD and Raman observations, that implied an increasing presence of Cr^{4+} with increasing incorporation of Cr in the as-prepared perovskites, see Section 2.1. The presence of Cr^{6+} has been previously reported in Cr-perovskites under oxidative conditions^[41], which in this case is very minor since SrCrO_4 was not detected by XRD neither in the pristine material, Fig. 2, nor in the cycled form, see Fig.S5 and S6 in Supporting Information. Comparing the spin orbitals peak position of the pristine vs. cycled samples, it can be observed negligible differences in the oxidation state of Cr on the surface of $\text{La}_{0.6}\text{Sr}_{0.4}\text{Cr}_{0.85}\text{Mn}_{0.15}\text{O}_3$ before and after isothermal cycling, see Fig.8e. Conversely, differences between the as-prepared and cycled $\text{La}_{0.6}\text{Sr}_{0.4}\text{Cr}_{0.85}\text{Mn}_{0.15}\text{O}_3$ exist in the oxidation state of Mn, as shown by the $\text{Mn}2p$ spectra in Fig.8e: Here, each $\text{Mn}2p$ spectrum was fitted with spin-orbital doublets centered at 641.3 and 652.5 eV (FWHM = 2.4 eV) respectively due to $\text{Mn}2p_{3/2}$ and $\text{Mn}2p_{1/2}$ of Mn^{3+} and spin-orbital doublets centered at 643.0 and 654.2 eV (FWHM = 2.4 eV) respectively ascribed to $\text{Mn}2p_{3/2}$ and $\text{Mn}2p_{1/2}$ of Mn^{4+} .^[67,68] The valence state of Mn was roughly 50:50 for Mn^{4+} and Mn^{3+} in as-synthesized $\text{La}_{0.6}\text{Sr}_{0.4}\text{Cr}_{0.85}\text{Mn}_{0.15}\text{O}_3$, Fig.8e. On the other hand, there was $\approx 20\%$ increase in Mn^{4+} after 15 isothermal cycles; this

increase in Mn valence could be a result of the high temperature for isothermal cycling as well as the oxidative environment at which the material is exposed in the last part of the longevity test (50% CO₂). The La3d and Sr3d spectra reveal that the valence of both La (*e.g.* La³⁺) and Sr (*e.g.* Sr²⁺) are consistent in as-prepared and cycled La_{0.6}Sr_{0.4}Cr_{0.85}Mn_{0.15}O₃, see Supporting Information Fig. S7. This result implies that Mn ions, along with Cr ions, are the active redox sites that participate in the oxygen exchange during thermochemical CO₂ splitting. Still, the valence states of La, Sr, and Cr are largely unchanged before and after the longevity test, which supports the observed retention in the catalytic activity of La_{0.6}Sr_{0.4}Cr_{0.85}Mn_{0.15}O₃. Thus, based on the 15 isothermal cycles test and the high degree of surface and microstructural stability corroborated by XPS, SEM, XRD and EDX, we can conclude that La_{0.6}Sr_{0.4}Cr_{0.85}Mn_{0.15}O₃ shows promise for thermochemical solar-to-fuel production at high temperatures.

3. Conclusions

Thermochemical fuel production suitable for solar-driven reactors was operated on the basis of the new La_{0.6}Sr_{0.4}Cr_xMn_{1-x}O₃ perovskite materials, which exhibit promising CO₂ fuel splitting rates at higher operation temperature for increase Cr-doping. The most favorable rate performance was observed for La_{0.6}Sr_{0.4}Cr_{0.85}Mn_{0.15}O₃, which showed 2-fold faster CO₂ splitting reaction than state-of-the-technology ceria, 1.5 and 0.8 mL min⁻¹ g⁻¹ respectively, when operated under isothermal cycles at 1400 °C. Furthermore, this material showed high thermochemical and structural stability and durability when tested under a 15 multi-cycle isothermal test at 1400 °C. Surface analysis of La_{0.6}Sr_{0.4}Cr_{0.85}Mn_{0.15}O₃ displayed small differences in the valence states of La, Sr, Cr, and Mn before and after 15 isothermal cycles,

implying that these perovskites mostly retain their surface chemistry under the reaction conditions, which is critical since Mn and Cr ions are the redox-active sites that participate in the oxygen exchange during the thermochemical catalysis. These results support the hypothesis that an enhanced thermodynamic driving force to split CO₂ exists, with increased Cr-content for the lanthanum strontium chromium manganese perovskites. Regarding the total fuel production, the optimal composition is La_{0.6}Sr_{0.4}Cr_{0.3}Mn_{0.7}O₃ operated under near-isothermal conditions, $T_{red}=1400\text{ }^{\circ}\text{C}/T_{ox}=1200\text{ }^{\circ}\text{C}$, which are also more efficient than pure isothermal cycling in terms of heat recuperation, excess of CO₂ needed and the operational mode for the reduction step.^[35]

In summary, we demonstrate on the example of La_{0.6}Sr_{0.4}Cr_{0.85}Mn_{0.15}O₃ that one can adapt the perovskite chemistry (i.e. doping of transition metal ions) to tune the thermochemical properties in order to meet the most optimum trade-off between fast kinetics and fuel production, which can also benefit from the most suitable near-isothermal/isothermal reactor schemes conditions. These are thus promising material candidates for solar-driven thermochemical fuel production and may give perspective to alternative reactor operation schemes.

4. Experimental Methods

4.1. Materials preparation

$\text{La}_{0.6}\text{Sr}_{0.4}\text{Cr}_x\text{Mn}_{1-x}\text{O}_3$ solid solutions ($0 < x < 0.85$) were synthesized using a modified version of the Pechini method. Citric acid (Sigma Aldrich, $\geq 99\%$) together with stoichiometric amounts of nitrate precursors, namely $\text{La}(\text{NO}_3)_3 \cdot 6\text{H}_2\text{O}$ (Sigma Aldrich, $\geq 99.99\%$), $\text{Sr}(\text{NO}_3)_2$ (Fluka Analytical, $\geq 99\%$), $\text{Cr}(\text{NO}_3)_3 \cdot 9\text{H}_2\text{O}$ (Sigma Aldrich, $\geq 97\%$) and $\text{Mn}(\text{NO}_3)_2 \cdot 4\text{H}_2\text{O}$ (Sigma Aldrich, $\geq 97\%$); were dissolved in deionized water at room temperature in a 60:40 ratio. Afterward, the aqueous solution was heated up to 80°C under constant stirring, followed by addition of ethylene glycol (Fluka Analytical, $\geq 98\%$) in a 2 to 3 weight ratio. Continuing the stirring and keeping the temperature at 80°C , water was evaporated until a gel was formed. The gel was then dried on a heating plate at 200°C for 2 hours followed by calcination for 1 hour at 400°C . The calcined gel was ground to fine powders in an agate mortar, and heat-treated inside an alumina crucible at 1250°C for 10 hours, setting a heating rate of $20^\circ\text{C min}^{-1}$. In order to avoid undesired chromate segregations, materials were calcined further at 1400°C for 24 hours. A list of the synthesized materials is given in Table 1. Commercial CeO_2 (Sigma Aldrich, nano-powder with an average grain size of 50nm, 99.95% purity) was employed as a benchmark.

4.2. Materials physicochemical characterization

X-ray powder diffraction data were collected with a Panalytical X'Pert PRO MPD diffractometer. $\text{Cu K}\alpha$ radiation ($\lambda = 1.5406 \text{ \AA}$; Ge monochromator) produced with an

extraction voltage of 45 kV at 40 mA current was used to scan the samples in a Bragg-Brentano geometry in the range of $20^\circ < 2\theta < 120^\circ$ with a spinning speed of 60 rot min^{-1} , a step width of 0.017° and irradiation time of 3 seconds. Panalytical HighScore Plus software was utilized for Rietveld fitting, considering a rhombohedral perovskite (165744-ICSD) model structure and fitting the experimental data with a Pseudo Voigt function.

Raman spectra were collected on a confocal WITec Alpha300 R Raman microscope instrument (WITec Germany) equipped with 532 nm laser, using the 100-fold magnification objective and laser power of 0.5 or 1 mW, with a spectral resolution of 0.36 cm^{-1} . Each single spectrum consisted of three accumulations with an integration of 10 seconds.

The microstructure and particle morphology were assessed on a Zeiss Merlin High-resolution SEM. An acceleration voltage of 7kV and Inlens detector were used. The same equipment was used for elemental characterization via Energy Dispersive X-ray spectroscopy (EDX) with an Octane Elect EDS System. The average particle size was determined using the software ImageJ.^[69]

Thermogravimetric analyses (TGA) were carried out on a NETZSCH 449C equipped with a set of mass flow controllers (Bronkhorst) allowing atmospheric control during the experiments. In order to determine the reduction extent (δ) of $\text{La}_{0.6}\text{Sr}_{0.4}\text{Cr}_x\text{Mn}_{1-x}\text{O}_3$ solid solutions, about 100 mg of perovskite powders were placed in a TGA alumina crucible (NETZSCH) and heated up to 1400°C under constant Ar flow of 100 ml min^{-1} , with heating and cooling rates of $20^\circ\text{C min}^{-1}$.

X-ray photoelectron spectroscopy (XPS) was performed on a Thermo K-Alpha XPS system with a spot size of $400 \mu\text{m}$ and a resolution of 0.1 eV. All spectra were processed and analyzed using Thermo Advantage, which is a software package provided through

ThermoScientific; the FWHM doublet splittings (where applicable), and peak positions were constant and fixed for all XPS deconvolutions.

4.3. Thermochemical cycling

The capacity of $\text{La}_{0.6}\text{Sr}_{0.4}\text{Cr}_x\text{Mn}_{1-x}\text{O}_3$ solid solutions for 2-step thermochemical CO_2 production was evaluated in a high-temperature fixed-bed reactor connected to a Raman laser gas analyzer (Atmospheric Recovery, Inc.). Fig.S8 illustrates the experimental reactor set up. It consists of a set of electric mass flow controllers (Voegtlin) that adjusted the desired gas compositions of inert or oxidizing gas to the alumina reactor (Nanoker, 800 mm length, 12 mm outer diameter), located inside a vertical tubular electrical furnace (HTRV 16/40/250/E3216CP/OTC, Carbolite Gero GmbH). About 1 g of perovskite material was placed in powder form over an alumina porous wool bed situated at the half-length of the alumina tube. Sample temperature was monitored by an S-type thermocouple in contact with the outer surface of the perovskite powder loose bed. The outlet gas stream was analyzed by a Raman laser gas analyzer, calibrated with premixed gas cylinders of known concentrations (zero gas bottle of Ar; reducing gas bottle 0.5% CH_4 , 0.5% H_2 , 0.5% CO balanced with Ar; oxidizing gas bottle with 5% O_2 , 15% CO_2 , balanced with N_2 , all 99.9999%, Airgas).

Thermochemical cycling runs for CO_2 splitting were specifically programmed for the evaluation of the temperature influence on the CO production kinetics. For that purpose, $\text{La}_{0.6}\text{Sr}_{0.4}\text{Cr}_x\text{Mn}_{1-x}\text{O}_3$ powder materials were screened under a cycling program consisting of eight alternating reduction and oxidation cycles. Before each experiment, a purging step with Ar was carried out to remove residual ambient air coming from off-operation periods. Then, the first three cycles evaluated the CO_2 splitting behavior at three isothermal temperatures

(1200, 1300, 1400 °C). After reaching the desired temperature, the reduction was performed for 30 min under a constant flow of 300 ml min⁻¹ of Ar (99.999% purity, Airgas). The total gas flow was always kept at this value based on the gas analyzer specifications atmosphere. After the reduction step, CO₂ (99.998%, Airgas) balanced with Ar was injected at a $p\text{CO}_2=0.5$ atm. The second part of the cycling test was performed under a temperature-swing scheme. Reduction was carried out at 1400 °C for 20 min, after which the temperature was cooled down to the desired value for the CO₂ splitting. After reaching the programmed temperatures (1000, 1100, 1200, 1300 °C), CO₂ was injected at the same concentration as for the three first cycles during 20 min. Finally, the material was subjected to a last isothermal cycle at 1400 °C. For every heating ramp, 50 °C min⁻¹ rates were used. The CO total production was obtained by integration of the CO production curves. For CO₂ splitting at high temperatures (1300-1400 °C) we subtracted the amount of CO generated by CO₂ thermolysis ($\text{CO}_2(\text{g}) \rightarrow \text{CO} + \frac{1}{2} \text{O}_2(\text{g})$) from the total CO produced by computing the O₂ produced during the thermolysis and obtaining the equivalent stoichiometric amount of CO, which was then subtracted from the total CO yield.

Acknowledgments

The authors acknowledge financial support by the ETH Foundation for this work; grant number ETH-05 13-1. The authors would like to thank Dr. R. Pfenninger for developing the setup control software, Patrick Boisvert for the help with EDX and Dr. C. Settens for the initial help with XRD refinement. This work made use of the MRSEC Shared Experimental Facilities at MIT, supported by the National Science Foundation under award number DMR-14-19807. In addition, the authors thank Prof. A. Studart, ETH Zurich, for the use of the TGA.

Authors Contributions

A.J.C, A.H.B and J.L.M.R conceived the project. A.H.B performed the thermodynamic calculations and interpretation. T.M. synthesized the materials. A.J.C. designed and built the reactor setup with help of A.H.B and T.M. T.M. and A.J.C. performed the reactor experiments, XRD, EDX and SEM. T.M. performed the TGA. T.M. and E.S. performed the Raman characterization and interpretation. Z.D.H performed the XPS characterization and interpretation. J.L.M.R. discussed and supervised the work. The paper was co-written by A.J.C., A.H.B and J.L.M.R., and all authors discussed the results and commented on the manuscript.

References

- [1] H. L. Tuller, *Mater. Renew. Sustain. Energy* **2017**, 6, 3.
- [2] C. N. R. Rao, S. Dey, *Proc. Natl. Acad. Sci.* **2017**, 114, 13385.
- [3] R. J. Carrillo, J. R. Scheffe, *Sol. Energy* **2017**, 156, 3.
- [4] A. H. McDaniel, *Curr. Opin. Green Sustain. Chem.* **2017**, 4, 37.
- [5] C. L. Muhich, B. D. Ehrhart, I. Al-Shankiti, B. J. Ward, C. B. Musgrave, A. W. Weimer, *Wiley Interdiscip. Rev. Energy Environ.* **2016**, 5, 261.
- [6] D. Marxer, P. Furler, M. Takacs, A. Steinfeld, *Energy Environ. Sci.* **2017**, 10, 1142.
- [7] S. Zhai, J. Rojas, N. Ahlborg, K. Lim, M. F. Toney, H. Jin, W. C. Chueh, A. Majumdar, *Energy Environ. Sci.* **2018**, 11, 2172.
- [8] M. Kubicek, A. H. Bork, J. L. M. Rupp, *J. Mater. Chem. A* **2017**, 5, 11983.
- [9] J. R. Scheffe, D. Weibel, A. Steinfeld, *Energy & Fuels* **2013**, 27, 4250.
- [10] C.-K. Yang, Y. Yamazaki, A. Aydin, S. M. Haile, *J. Mater. Chem. A* **2014**, 2, 13612.
- [11] M. J. Ignatowich, A. H. Bork, T. C. Davenport, J. L. M. Rupp, C. Yang, Y. Yamazaki, S. M. Haile,

- [12] A. H. Bork, E. Povoden-Karadeniz, J. L. M. Rupp, *Adv. Energy Mater.* **2017**, 7, 1601086.
- [13] S. Dey, B. S. Naidu, C. N. R. Rao, *Dalt. Trans.* **2016**, 45, 2430.
- [14] S. Dey, B. S. Naidu, A. Govindaraj, C. N. R. Rao, *Phys. Chem. Chem. Phys.* **2015**, 17, 122.
- [15] S. Dey, B. S. Naidu, C. N. R. Rao, *Chem. A Eur. J.* **2015**, 21, 7077.
- [16] A. Demont, S. Abanades, *RSC Adv.* **2014**, 4, 54885.
- [17] A. Demont, S. Abanades, *J. Mater. Chem. A* **2015**, 3, 3536.
- [18] J. Vieten, B. Bulfin, P. Huck, M. Horton, D. Guban, L. Zhu, Y. Lu, K. A. Persson, M. Roeb, C. Sattler, *Energy Environ. Sci.* **2019**, 12, 1369.
- [19] D. R. Barcellos, M. D. Sanders, J. Tong, A. H. McDaniel, R. P. O'Hayre, *Energy Environ. Sci.* **2018**, 11, 3256.
- [20] A. Riaz, P. Kreider, F. Kremer, H. Tabassum, J. S. Yeoh, W. Lipiński, A. Lowe, *ACS Appl. Energy Mater.* **2019**, 2, 2494.
- [21] D. Papargyriou, J. T. S. Irvine, *Solid State Ionics* **2016**, 288, 120.
- [22] S. Tao, J. T. S. Irvine, *J. Electrochem. Soc.* **2004**, 151, A252.
- [23] S. Boulfrad, M. Cassidy, E. Djurado, J. T. S. Irvine, G. Jabbour, *Int. J. Hydrogen Energy* **2013**, 38, 9519.
- [24] Tao, J. T. S. Irvine, S. M. Plint, *J. Phys. Chem. B* **2006**, 110, 21771.
- [25] A. H. Bork, Perovskites as Material Class for 2-step Thermochemical Solar to-Fuel Conversion. Using Thermodynamic Principles for Design and Assessment of New Materials, PhD Dissertation, ETH Zurich, 2017.
- [26] J. Mizusaki, H. Tagawa, K. Naraya, T. Sasamoto, *Solid State Ionics* **1991**, 49, 111.
- [27] J. Mizusaki, S. Yamauchi, K. Fueki, A. Ishikawa, *Solid State Ionics* **1984**, 12, 119.
- [28] A. H. Bork, M. Kubicek, M. Struzik, J. L. M. Rupp, *J. Mater. Chem. A* **2015**, 3, 15546.
- [29] E. Povoden-Karadeniz, M. Chen, T. Ivas, A. N. Grundy, L. J. Gauckler, *J. Mater. Res.* **2012**, 27, 1915.
- [30] C. L. Muhich, B. W. Evanko, K. C. Weston, P. Lichty, X. Liang, J. Martinek, C. B. Musgrave, A. W. Weimer, *Science* **2013**, 341, 540.
- [31] M. Tou, R. Michalsky, A. Steinfeld, *Joule* **2017**, 1, 146.
- [32] B. J. Hathaway, R. Bala Chandran, A. C. Gladen, T. R. Chase, J. H. Davidson, *Energy and Fuels* **2016**, 30, 6654.
- [33] Y. Hao, C.-K. Yang, S. M. Haile, *Phys. Chem. Chem. Phys.* **2013**, 15, 17084.
- [34] S. Dey, C. N. R. Rao, *ACS Energy Lett.* **2016**, 1, 237.
- [35] I. Al-Shankiti, B. D. Ehrhart, A. W. Weimer, *Sol. Energy* **2017**, 156, 21.
- [36] Q. Jiang, J. Tong, G. Zhou, Z. Jiang, Z. Li, C. Li, *Sol. Energy* **2014**, 103, 425.
- [37] A. H. McDaniel, E. C. Miller, D. Arifin, A. Ambrosini, E. N. Coker, R. O'Hayre, W. C. Chueh, J. Tong, *Energy Environ. Sci.* **2013**, 6, 2424.

- [38] B. D. Ehrhart, C. L. Muhich, I. Al-Shankiti, A. W. Weimer, *Int. J. Hydrogen Energy* **2016**, *41*, 19881.
- [39] L. Vegard, *Zeitschrift für Phys.* **1921**, *5*, 17.
- [40] R. D. Shannon, *Acta Crystallogr. Sect. A* **1976**, *32*, 751.
- [41] V. B. Vert, F. V. Melo, L. Navarrete, J. M. Serra, *"Applied Catal. B, Environ.* **2012**, *115–116*, 346.
- [42] M. N. Iliev, M. V. Abrashev, V. N. Popov, V. G. Hadjiev, *Phys. Rev. B - Condens. Matter Mater. Phys.* **2003**, *67*, 3.
- [43] M. N. Iliev, A. P. Litvinchuk, V. G. Hadjiev, Y.-Q. Wang, J. Cmaidalka, R.-L. Meng, Y.-Y. Sun, N. Kolev, M. V. Abrashev, *Phys. Rev. B* **2006**, *74*, 214301.
- [44] A. Dubroka, J. Humlíček, M. V. Abrashev, Z. V. Popović, F. Sapiña, A. Cantarero, *Phys. Rev. B - Condens. Matter Mater. Phys.* **2006**, *73*, 1.
- [45] J. Andreasson, J. Holmlund, C. S. Knee, M. Käll, L. Börjesson, S. Naler, J. Bäckström, M. Rübhausen, A. K. Azad, S. G. Eriksson, *Phys. Rev. B - Condens. Matter Mater. Phys.* **2007**, *75*, 1.
- [46] M. Vračar, A. Kuzmin, R. Merkle, J. Purans, E. A. Kotomin, J. Maier, O. Mathon, *Phys. Rev. B - Condens. Matter Mater. Phys.* **2007**, *76*, 1.
- [47] C. L. Bull, P. F. McMillan, *J. Solid State Chem.* **2004**, *177*, 2323.
- [48] A. G. Souza Filho, J. L. B. Faria, I. Guedes, J. M. Sasaki, P. T. C. Freire, V. N. Freire, J. Mendes Filho, M. M. Xavier, F. A. O. Cabral, J. H. de Araújo, J. A. P. da Costa, *Phys. Rev. B* **2003**, *67*, 052405.
- [49] Y. Fujioka, J. Frantti, M. Kakihana, *J. Phys. Chem. B* **2004**, *108*, 17012.
- [50] G. Kotnana, S. N. Jammalamadaka, *J. Appl. Phys.* **2015**, *118*, 1.
- [51] I. G. Siny, R. S. Katiyar, a S. Bhalla, *J. Raman Spectrosc.* **1998**, *29*, 385.
- [52] A. A. Yaremchenko, A. V. Kovalevsky, V. V. Kharton, *Solid State Ionics* **2008**, *179*, 2181.
- [53] R. Saravanan, N. Thenmozhi, Y. P. Fu, *Phys. B Condens. Matter* **2016**, *493*, 25.
- [54] S. P. Jiang, J. P. Zhang, K. Foger, *J. Electrochem. Soc.* **2000**, *147*, 3195.
- [55] S. P. Jiang, S. Zhang, Y. D. Zhen, *J. Electrochem. Soc.* **2006**, *153*, A127.
- [56] C. L. Muhich, K. C. Weston, D. Arifin, A. H. McDaniel, C. B. Musgrave, A. W. Weimer, *Ind. Eng. Chem. Res.* **2015**, *54*, 4113.
- [57] T. Cooper, J. R. Scheffe, M. E. Galvez, R. Jacot, G. Patzke, A. Steinfeld, *Energy Technol.* **2015**, *3*, 1130.
- [58] M. Takacs, M. Hoes, M. Caduff, T. Cooper, J. R. Scheffe, A. Steinfeld, *Acta Mater.* **2016**, *103*, 700.
- [59] Q. Jiang, Z. Chen, J. Tong, M. Yang, Z. Jiang, C. Li, *Chem. Commun.* **2017**, *53*, 1188.
- [60] B. Bulfin, *Phys. Chem. Chem. Phys.* **2019**, 2186.
- [61] D. Marxer, P. Furler, J. Scheffe, H. Geerlings, C. Falter, V. Batteiger, A. Sizmann, A. Steinfeld, *Energy & Fuels* **2015**, *29*, 3241.
- [62] M. Takacs, J. R. Scheffe, A. Steinfeld, *Phys. Chem. Chem. Phys.* **2015**, *17*, 7813.
- [63] T. C. Davenport, M. Kemei, M. J. Ignatowich, S. M. Haile, *Int. J. Hydrogen Energy* **2017**, *42*, 16932.
- [64] I. Al-Shankiti, B. D. Ehrhart, A. W. Weimer, *Sol. Energy* **2017**.

- [65] I. Ikemoto, K. Ishii, S. Kinoshita, H. Kuroda, M. A. Alario Franco, J. M. Thomas, *J. Solid State Chem.* **1976**, *17*, 425.
- [66] G. P. Halada, C. R. Clayton, *J. Electrochem. Soc.* **1991**, *138*, 2921.
- [67] J. Moulder, W. Stickle, P. Sobol, K. Bomben, *Handbook of X-ray photoelectron spectroscopy*; 1992.
- [68] Q. H. Wu, M. Liu, W. Jaegermann, *Mater. Lett.* **2005**, *59*, 1480.
- [69] C. A. Schneider, W. S. Rasband, K. W. Eliceiri, *Nat. Methods* **2012**, *9*, 671.

Table 1. Formula, lattice volume and average particle size of the $\text{La}_{0.6}\text{Sr}_{0.4}\text{Cr}_x\text{Mn}_{1-x}\text{O}_3$ materials.

Formula	Label	Lattice Volume (\AA^3)	Avg. Particle size (μm)
$\text{La}_{0.6}\text{Sr}_{0.4}\text{MnO}_3$	LSM	348.05	1.5 ± 0.5
$\text{La}_{0.6}\text{Sr}_{0.4}\text{Cr}_{0.1}\text{Mn}_{0.9}\text{O}_3$	LSCM10	347.03	2.4 ± 0.8
$\text{La}_{0.6}\text{Sr}_{0.4}\text{Cr}_{0.3}\text{Mn}_{0.7}\text{O}_3$	LSCM30	345.57	2.5 ± 0.7
$\text{La}_{0.6}\text{Sr}_{0.4}\text{Cr}_{0.5}\text{Mn}_{0.5}\text{O}_3$	LSCM50	344.33	2.2 ± 0.7
$\text{La}_{0.6}\text{Sr}_{0.4}\text{Cr}_{0.75}\text{Mn}_{0.25}\text{O}_3$	LSCM75	343.94	1.9 ± 0.5
$\text{La}_{0.6}\text{Sr}_{0.4}\text{Cr}_{0.85}\text{Mn}_{0.15}\text{O}_3$	LSCM85	344.22	1.7 ± 0.6

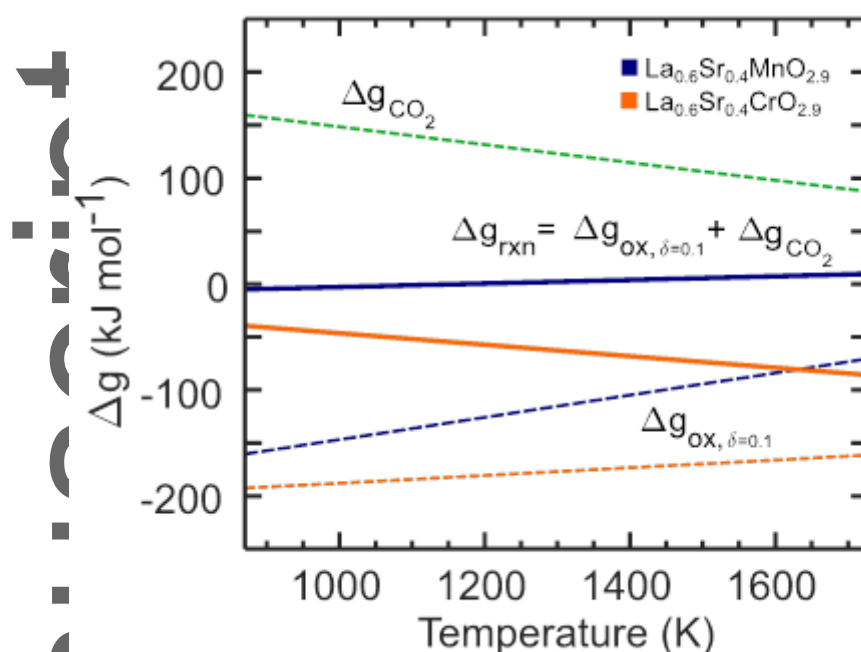


Figure 1. Thermodynamics for CO₂ splitting of La_{0.6}Sr_{0.4}MnO_{3-δ} (blue) and La_{0.6}Sr_{0.4}CrO_{3-δ} (orange) perovskites, which serve as a rationale for testing the La_{0.6}Sr_{0.4}Cr_xMn_{1-x}O_{3-δ} solid solutions. The green dashed line corresponds to the Gibbs energy change for the CO₂ splitting reaction (Δg_{CO_2}) with temperature, data extracted from HSC Chemistry 6.1 from Outotec Research Oy. The dashed lines represent the Gibbs free energy change of oxidation by oxygen (Δg_{ox}) for the perovskite at an oxygen nonstoichiometry of $\delta=0.1$, calculated with data extracted from Ref. [26,27]. The blue and orange solid lines represent the Gibbs free energy for the CO₂ splitting reaction with the La_{0.6}Sr_{0.4}MnO_{3-δ} and La_{0.6}Sr_{0.4}CrO_{3-δ} perovskites (Δg_{rxn}), respectively. The properties of La_{0.6}Sr_{0.4}Cr_xMn_{1-x}O_{3-δ} solid solutions are expected to lie in between the lines of the end-members.

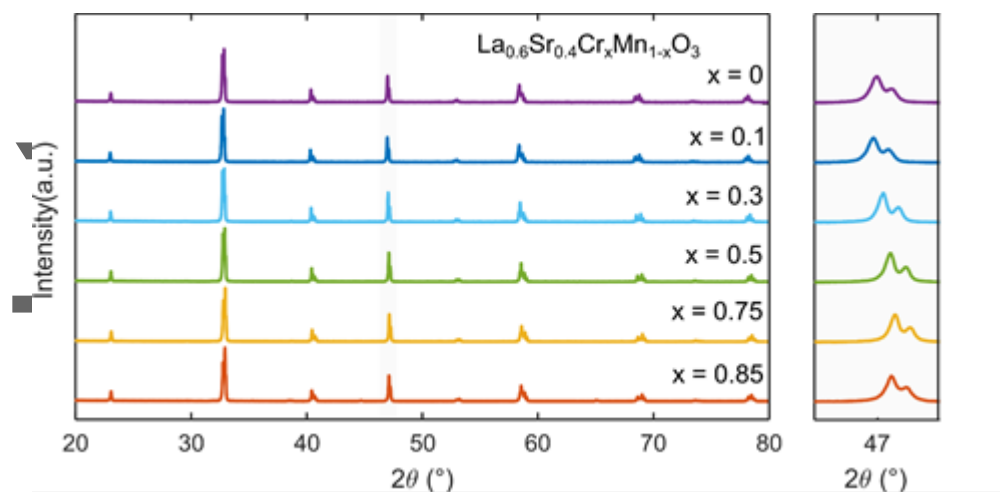


Figure 2: X-ray diffraction patterns of the as-synthesized $\text{La}_{0.6}\text{Sr}_{0.4}\text{Cr}_x\text{Mn}_{1-x}\text{O}_3$ materials. The grey shadowed area was zoomed out on the right panel in order to compare the shift of the reflection around $2\theta=47^\circ$ due to partial substitution of Mn cations by Cr cations.

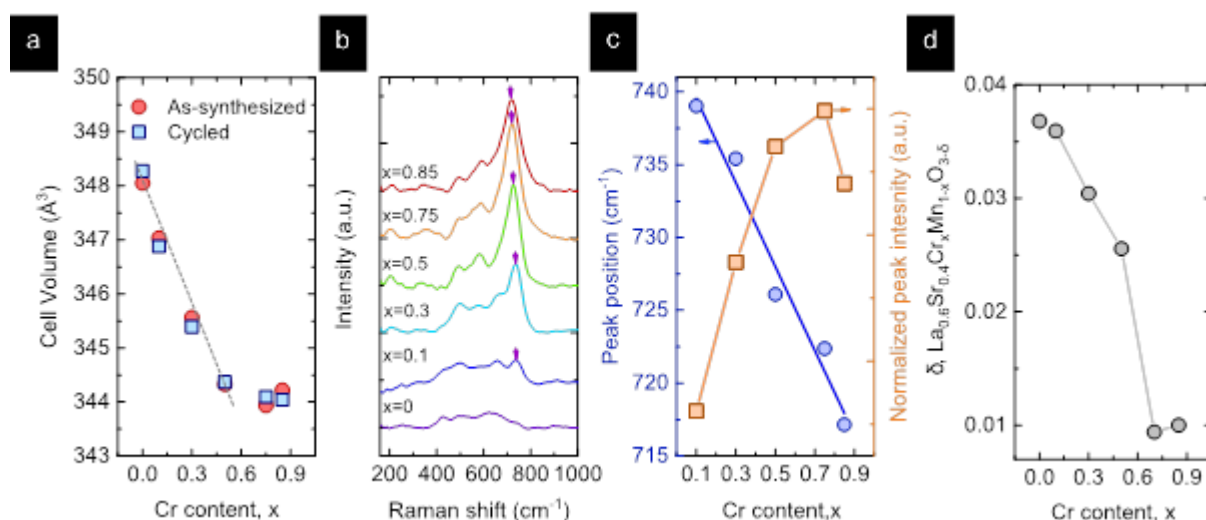


Figure 3. (a) Cell volume values of $\text{La}_{0.6}\text{Cr}_{0.4}\text{Cr}_x\text{Mn}_{1-x}\text{O}_3$ perovskite materials with varying Cr concentration before and after cycling: XRD, cell volume parameters were obtained by Rietveld refinement. The grey-dashed line shows the linear regression between $x=0$ and $x=0.5$ compositional range that follows Vegard's law. (b) Raman spectra of $\text{La}_{0.6}\text{Sr}_{0.4}\text{Cr}_x\text{Mn}_{1-x}\text{O}_3$ samples before cycling. Spectra were acquired at room temperature with a 532 nm laser. The arrows show the position of the band ascribed to A_g -like mode. (c) Plot showing the peak position of the band assigned to A_g -like lattice vibration and its normalized intensity versus the Cr concentration, x , in $\text{La}_{0.6}\text{Cr}_{0.4}\text{Cr}_x\text{Mn}_{1-x}\text{O}_3$. (d) Oxygen non-stoichiometry for $\text{La}_{0.6}\text{Sr}_{0.4}\text{Cr}_x\text{Mn}_{1-x}\text{O}_3$ materials determined by thermogravimetric analyses. Perovskite powders were heated up to 1400 °C under Ar atmosphere.

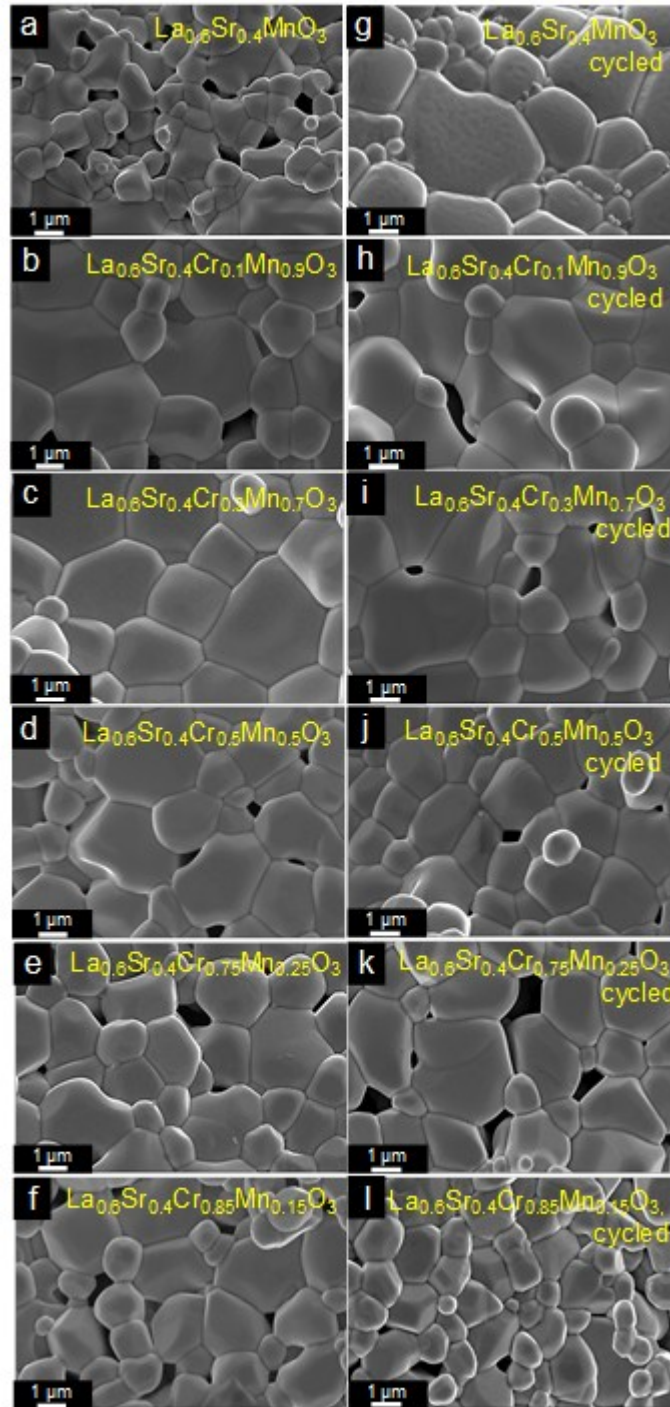


Figure 4: SEM micrographs of (a-f) as-synthesized and (g-l) cycled $\text{La}_{0.6}\text{Sr}_{0.4}\text{Cr}_x\text{Mn}_{1-x}\text{O}_3$ powders. (a) $x=0$, (b) $x=0.1$, (c) $x=0.3$, (d) $x=0.5$, (e) $x=0.75$ and (f) $x=0.85$.

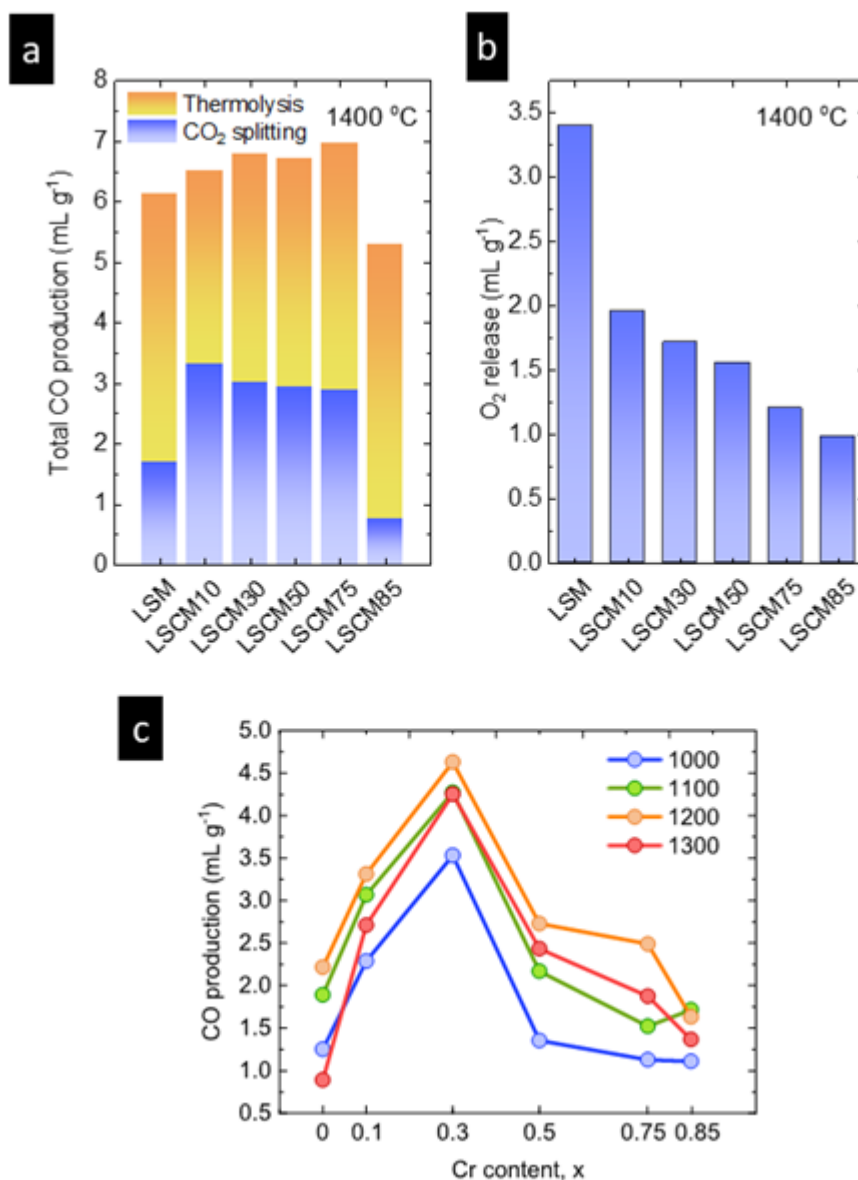


Figure 5. (a) Total CO production for the isothermal cycle at 1400 °C and $p\text{CO}_2=0.5$ atm, differentiating the contribution of the CO produced from the 2-step CO₂ splitting half-cycle (blue color) and the CO generated via the thermo-catalytic cracking of CO₂ (orange). (b) Oxygen release at 1400 and constant flow of Ar 300 mL min⁻¹. Values extracted from the integration of the O₂ curve of the fifth reduction half-cycle. (c) Influence of the Cr content, x, in the CO production for the temperature-swing cycles of La_{0.6}Sr_{0.4}Cr_xMn_{1-x}O₃ perovskites. Only the CO coming from the CO₂ splitting reaction is computed.

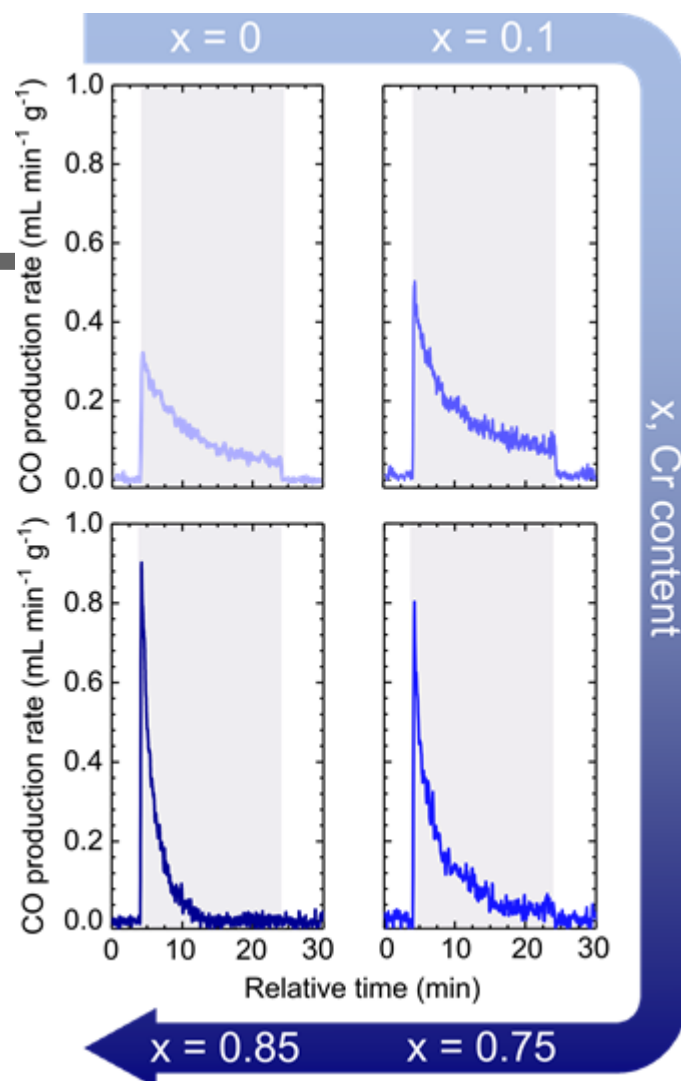


Figure 6. CO production rates of $\text{La}_{0.6}\text{Sr}_{0.4}\text{Cr}_x\text{Mn}_{1-x}\text{O}_3$ materials obtained for the CO_2 splitting half-cycle performed at $1200\text{ }^\circ\text{C}$ and $p\text{CO}_2=0.5\text{ atm}$, previously materials were reduced at $1400\text{ }^\circ\text{C}$ under Ar atmosphere. Compositional end-members were plotted for the sake of understanding the impact of Cr incorporation in the perovskite. The grey-shaded area indicates the 20 min CO_2 injection.

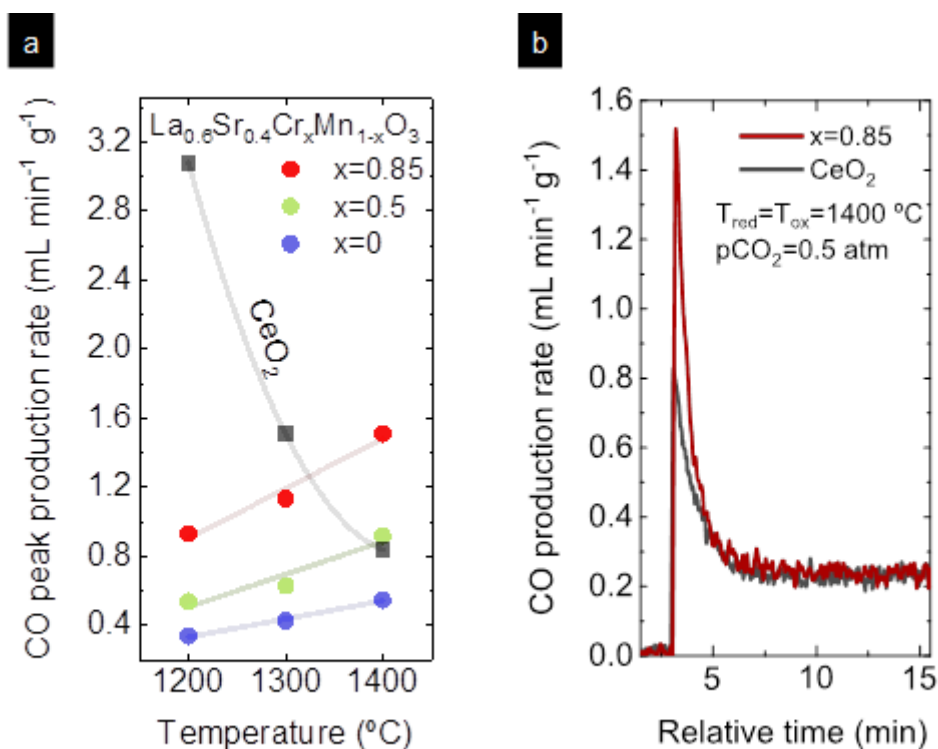


Figure 7. (a) CO production rate peak-values determined at temperatures relevant to near- and isothermal splitting cycles. Here, the oxides were previously reduced at 1400 °C under Ar atmosphere and then cooled down (or maintained) to the CO₂ splitting temperature, 1200-1400 °C. For the sake of comparison, results for the compositional end-members, La_{0.6}Sr_{0.4}MnO₃ (LSM) and La_{0.6}Sr_{0.4}Cr_{0.85}Mn_{0.15}O₃ (LSCM85); La_{0.6}Sr_{0.4}Cr_{0.5}Mn_{0.5}O₃ (LSCM50) and CeO₂ are plotted. Fitting curves are just used as a visual guide. (b) Comparison of the CO production profiles of La_{0.6}Sr_{0.4}Cr_{0.85}Mn_{0.15}O₃ (LSCM85) and commercial ceria at 1400 °C. Note that the catalytic contribution of CO₂ thermolysis has not been subtracted for the sake of comparison.

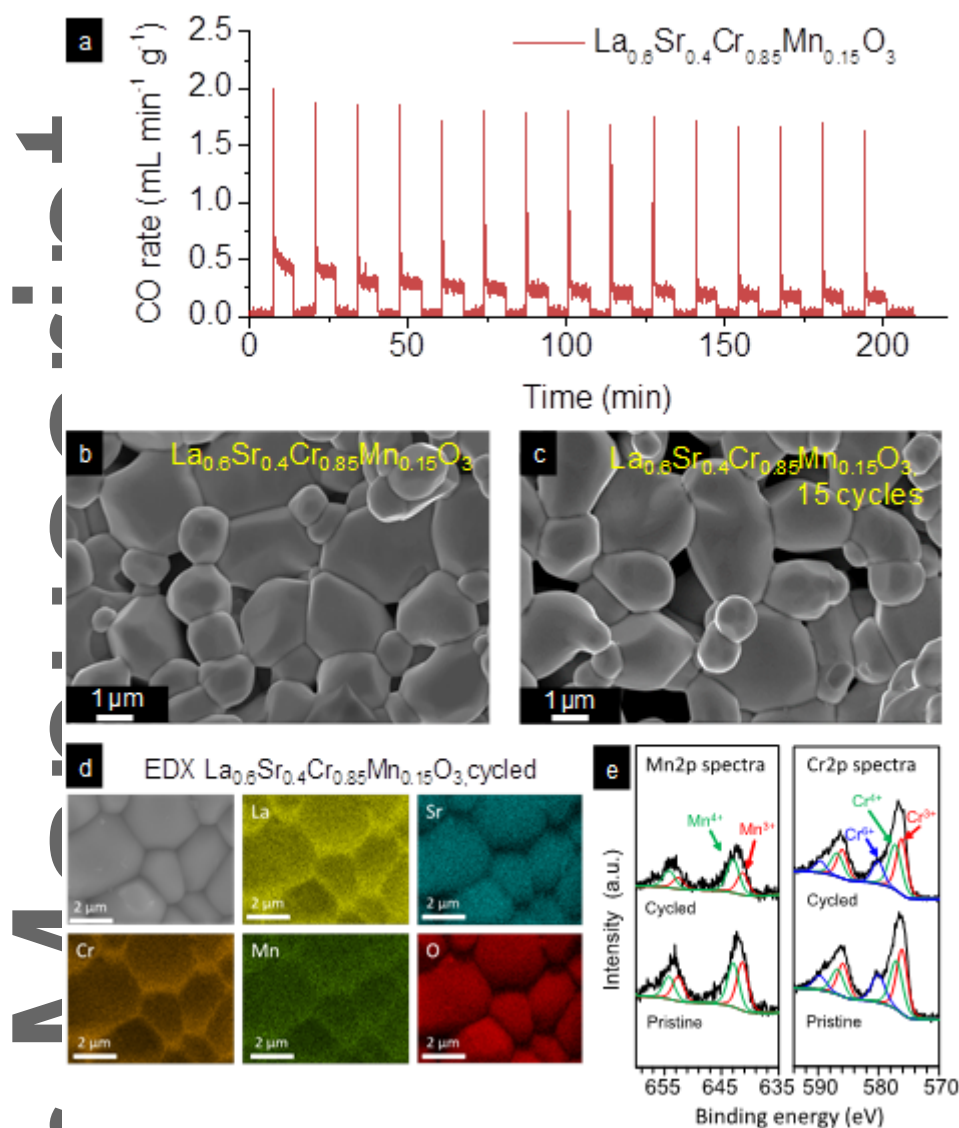
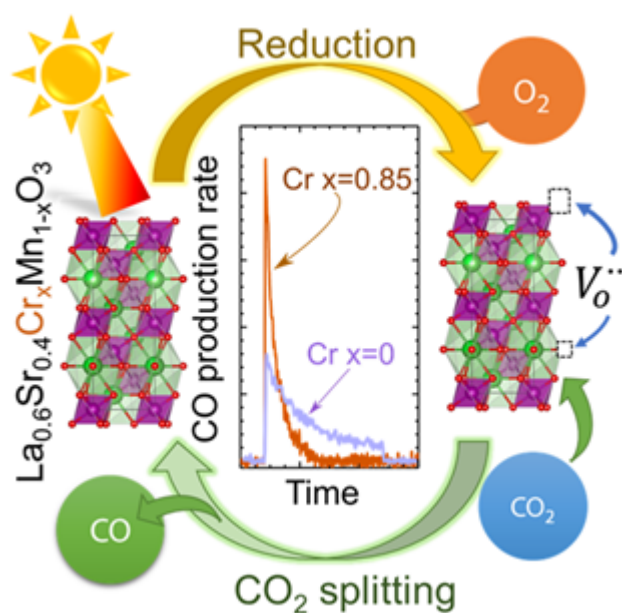


Figure 8. (a) CO production rate observed during a longevity test carried out to La_{0.6}Sr_{0.4}Cr_{0.85}Mn_{0.15}O₃ consisting of 15 isothermal cycles at 1400 °C. Reduction was performed under of Ar atmosphere and CO₂ splitting steps using a mixture of 50% CO₂ balanced with Ar, maintaining always the flow at 300 mL min⁻¹. (b-c) SEM micrographs comparing the morphology between as-synthesized and cycled La_{0.6}Sr_{0.4}Cr_{0.85}Mn_{0.15}O₃. (d) EDX mapping of the cycled La_{0.6}Sr_{0.4}Cr_{0.85}Mn_{0.15}O₃. (e) Mn2p and Cr2p XPS comparison between La_{0.6}Sr_{0.4}Cr_{0.85}Mn_{0.15}O₃ before and after cycling.

ToC Figure



Targeted Size 55mmx50mm

ToC text

It is demonstrated that incorporation of Cr cations partially substituting Mn in La_{0.6}Sr_{0.4}Cr_xMn_{1-x}O₃ improves the CO₂ splitting rate in solar-driven thermochemical cycles for syngas production. CO production is especially enhanced under isothermal cycling schemes, $T_{red}=T_{ox}=1400$ °C, with $x=0.85$ exhibiting 3-fold faster reaction rates than $x=0$ and 2-fold faster than CeO₂.

ToC Keyword

Solar fuels